Article

Wheat Yellow Rust Detection Using UAV-Based Hyperspectral Technology

Anting Guo [1,2], Wenjiang Huang [1,2,3,*], Yingying Dong [1,2], Huichun Ye [1,3], Huiqin Ma [1], Bo Liu [4], Wenbin Wu [5], Yu Ren [1,2], Chao Ruan [1,2] and Yun Geng [1,2]

1 Key Laboratory of Digital Earth Science, Aerospace Information Research Institute, Chinese Academy of Sciences, Beijing 100094, China; guoat@aircas.ac.cn (A.G.); dongyy@radi.ac.cn (Y.D.); yehc@radi.ac.cn (H.Y.); mahq@aircas.ac.cn (H.M.); renyu@aircas.ac.cn (Y.R.); ruanchao@aircas.ac.cn (C.R.); gengyun17@mails.ucas.ac.cn (Y.G.)
2 University of Chinese Academy of Sciences, Beijing 100190, China
3 Key Laboratory of Earth Observation, Sanya 572029, China
4 State Key Laboratory for Biology of Plant Diseases and Insect Pests, Institute of Plant Protection, Chinese Academy of Agriculture Sciences, No.2 West Yuanmingyuan Road, Beijing 100193, China; bliu@ippcaas.cn
5 Chinese Academy of Agriculture Sciences, Beijing 100081, China; wuwenbin@caas.cn
* Correspondence: huangwj@aircas.ac.cn; Tel.: +86-10-82178169

Abstract: Yellow rust is a worldwide disease that poses a serious threat to the safety of wheat production. Numerous studies on near-surface hyperspectral remote sensing at the leaf scale have achieved good results for disease monitoring. The next step is to monitor the disease at the field scale, which is of great significance for disease control. In our study, an unmanned aerial vehicle (UAV) equipped with a hyperspectral sensor was used to obtain hyperspectral images at the field scale. Vegetation indices (VIs) and texture features (TFs) extracted from the UAV-based hyperspectral images and their combination were used to establish partial least-squares regression (PLSR)-based disease monitoring models in different infection periods. In addition, we resampled the original images with 1.2 cm spatial resolution to images with different spatial resolutions (3 cm, 5 cm, 7 cm, 10 cm, 15 cm, and 20 cm) to evaluate the effect of spatial resolution on disease monitoring accuracy. The findings showed that the VI-based model had the highest monitoring accuracy ($R^2 = 0.75$) in the mid-infection period. The TF-based model could be used to monitor yellow rust at the field scale and obtained the highest R^2 in the mid- and late-infection periods (0.65 and 0.82, respectively). The VI-TF-based models had the highest accuracy in each infection period and outperformed the VI-based or TF-based models. The spatial resolution had a negligible influence on the VI-based monitoring accuracy, but significantly influenced the TF-based monitoring accuracy. Furthermore, the optimal spatial resolution for monitoring yellow rust using the VI-TF-based model in each infection period was 10 cm. The findings provide a reference for accurate disease monitoring using UAV hyperspectral images.

Keywords: UAV hyperspectral; wheat yellow rust; disease monitoring; vegetation index; texture; spatial resolution

Publisher's Note: MDPI stays neutral with regard to jurisdictional claims in published maps and institutional affiliations.

1. Introduction

As one of the three major grain crops (wheat, rice, and corn) in China, wheat is the key to national food strategic security [1,2]. However, crop pests and diseases (more than 20 common ones) seriously endanger the safety of wheat production [3]. Yellow rust caused by *Puccinia striiformis f.* sp. *tritici* (Pst) causes explosive disease outbreaks and regional epidemics [4]. In epidemic years, yellow rust can reduce wheat yield by more than 40% or total harvest failure [5]. Therefore, the control of wheat yellow rust is crucial for food security. Only by accurately monitoring wheat diseases can we effectively prevent and control them and minimize losses. Traditionally, crop diseases have been assessed using visual monitoring, which has major limitations including small coverage and the inevitable

subjectivity of investigators [6]. Therefore, an effective and nondestructive monitoring method for crop diseases is needed to replace the traditional method.

After years of development, remote sensing has become an effective technology for monitoring crop diseases [7–11]. The advantage of remote sensing is that the spatial distribution of crop diseases can be assessed at low cost, allowing for better disease control [12]. Hyperspectral remote sensing is a relatively advanced technology. Compared with multispectral technology, it can provide rich narrow-band information. Previous studies have discussed the advantages of hyperspectral remote sensing in various applications compared with multispectral. For instance, Awad [13] made a comparison between multispectral and hyperspectral images in forest mapping and the results showed that the accuracies based on the hyperspectral image were much higher than that of the multispectral image. Yang et al. [14] compared the performance of airborne multispectral and hyperspectral imagery in mapping cotton root rot. Mariotto et al. [15] compared the performance of hyperspectral and multispectral data in terms of crop productivity modeling and type discrimination. The advantage of hyperspectral technology in crop disease monitoring is that it can capture certain physiological changes (e.g., pigments and water content) caused by diseases. In previous studies, many crop diseases have been monitored by hyperspectral remote sensing including wheat yellow rust [16,17], powdery mildew [18], fusarium head blight [3], peanut leaf spot disease [19], tomato spotted wilt virus [20], and rice bacterial leaf blight [21].

Vegetation indices (VIs) have demonstrated good performance for crop disease monitoring in previous research. For instance, Mahlein et al. [22] successfully identified sugar beet rust and powdery mildew based on some newly constructed spectral disease indices. Zheng et al. [2] used the re-established the photochemical reflectance index (PRI) based on 570 nm, 525 nm, and 705 nm, and anthocyanin reflectance index (ARI) based on 860 nm, 790 nm, and 750 nm to identify yellow rust. The results showed that PRI and ARI had good performance in the early–mid and mid–late growth stages of wheat, respectively. Liu et al. [23] developed a novel red-edge head blight index (REHBI) for monitoring wheat fusarium head blight at a regional scale. The VI is sensitive to the physiological changes inside the leaves caused by diseases, but cannot represent the changes in the surface characteristics of leaves. Texture is a feature that reflects external changes caused by diseases and is proven to have good performance in crop disease monitoring [24]. Previous studies have combined spectral and texture features to improve the ability to characterize diseases. For example, Guo et al. [25] combined texture and spectrum to identify wheat yellow rust on the leaf scales. The results showed that the model based on combined features had better performance than the model based on a single-feature. Al-Saddik et al. [26] successfully identified the yellowness on grapevine leaves using a combined feature (texture and spectral). The accuracy was 99% for both diseases when spectral and texture features were combined in the model. These studies confirm the effectiveness of VIs, texture features (TFs), and their combination for crop disease monitoring. However, previous studies on the fusion of spectral and image features to detect crop diseases have mostly been conducted at the leaf scale, and the feasibility of the method for disease detection at the field scale has not been confirmed.

The technology of unmanned aerial vehicles (UAV) may bring new opportunities for precision agriculture, especially in field-scale crop disease monitoring [27,28]. The advantage of an UAV lies in its flexibility, which can fly at any time under suitable conditions [29]. In general, images with ultra-high spatial and temporal resolution can be acquired by UAV systems in a cost-effective manner [30]. RGB, multispectral, and hyperspectral sensors can all be mounted on UAVs [31]. However, only hyperspectral sensors can simultaneously obtain high spatial and spectral resolution, providing advantages over RGB and multispectral sensors [32]. For instance, Abdulridha et al. [33] extracted VIs from UAV-based hyperspectral images to detect diseases in tomato. The authors concluded that the PRI and the normalized difference vegetation index (NDVI 850) could identify bacterial spot in all stages of disease development. Moreover, Abdulridha et al. [12,34] successfully detected citrus canker disease

and squash powdery mildew disease using a UAV-based hyperspectral imaging technique. Deng et al. [35] successfully detected citrus Huanglongbing based on UAV hyperspectral technology. The above studies confirm that UAV technology has good performance for crop disease monitoring; however, few studies have investigated the detection of yellow rust based on UAV hyperspectral images.

Spatial resolution of an image is determined by the instantaneous field of view (IFOV) and altitude of platform [36], which affects the efficiency of image collection and processing [37]. Generally, for the same sensor, the higher the altitude of the platform, the lower the spatial resolution [38]. It is crucial to select optimal spatial resolution according to observation object and specific requirements [39,40]. Few previous studies have focused on the impact of UAV-based image spatial resolution on target detection. Dash et al. [41] used UAV imagery with different resolutions to monitor forest disease outbreaks. They resampled the original images (0.06 m resolution) to new images (0.3, 1, and 3 m) and found that the optimal spatial resolution was 1 m for monitoring forest disease. Zhang et al. [42] assessed the impact of the spatial resolution for monitoring seedling rapeseed. Images with 1.35 cm, 1.69 cm, 2.61 cm, 5.73 cm, and 11.61 cm spatial resolutions were obtained by a UAV at different flying heights of 22 m, 29 m, 44 m, 88 m, and 176 m, respectively. The results showed that 2.61 cm was the optimal spatial resolution for monitoring seedling rapeseed growth. Liu et al. [43] used UAV images with different spatial resolutions to classify vegetation types and concluded that the classification accuracies exhibited slight fluctuations with a decrease in spatial resolution, and obtained the highest value when the spatial resolution was at an intermediate level. Although several studies have explored the effect of spatial resolution on detecting different ground objects, to date, no research has focused on the impact of different spatial resolutions for monitoring crop diseases, especially wheat yellow rust. Due to the limited ground coverage of UAV images, the optimal spatial resolution is an important aspect of the accurate detection of crop diseases.

In this research, a UAV equipped with a hyperspectral sensor was employed to monitor wheat yellow rust in multiple infection stages at different spatial scales. The objectives were to (1) evaluate the performance of monitoring wheat yellow rust at the field scale using VIs, TFs, and their combination obtained from UAV hyperspectral images; (2) determine the optimal image spatial resolution for monitoring wheat yellow rust with UAV images; and (3) use the optimal features and optimal spatial resolution to establish a monitoring model for yellow rust at the field scale in the early infection stage, mid-infection stage, and late infection stage.

2. Materials and Methods

2.1. Study Site

The UAV observation experiments of wheat yellow rust were carried out at the Langfang Experimental Station (39°30′41″N, 116°36′17″E) of the Chinese Academy of Agricultural Sciences; the station belongs to Langfang City, Hebei Province, China. The average annual temperature and precipitation in this area are 12 °C and 550 mm, respectively. The organic matter content, available phosphorus, and available potassium of the soil in the experimental area is about 1.41–1.47%, 20.5–55.8 mg·kg^{-1}, and 117.2–129.3 mg·kg^{-1}, respectively. 'Mingxian 169', which is a wheat cultivar susceptible to yellow rust, was selected for planting in the experimental area. Three plots were set up in the experimental area including two inoculated plots (A and B in Figure 1c) and one healthy plot (C in Figure 1c), each with an area of 220 m^2. In each plot, we set up eight sample collection regions, each with an area of 1 m^2. Wheat yellow rust fungus (spores) prepared in advance were mixed with water to form a spore suspension with a concentration of 9 mg/100 mL^{-1}. The suspension was sprayed on the wheat leaves with a handheld sprayer. The wheat was then quickly covered with plastic film, which was removed the next morning. The inoculation process followed the Rules for Resistance Evaluation of Wheat to Diseases and Insect Pests—Part 1: Rule for Resistance Evaluation of Wheat to Yellow Rust (NY/T 1443.1-2007). Pesticides were used to spray the wheat in the healthy plot to prevent it from being infected with yellow rust. In addition, the

wheat in all plots was managed in the same manner throughout the growth period including the application of the same amount of nitrogen and water. The location of the experimental area and the settings of the three experimental plots are shown in Figure 1. Figure 1c is an image of the entire experimental field obtained on 30 May using a UAV equipped with a hyperspectral sensor.
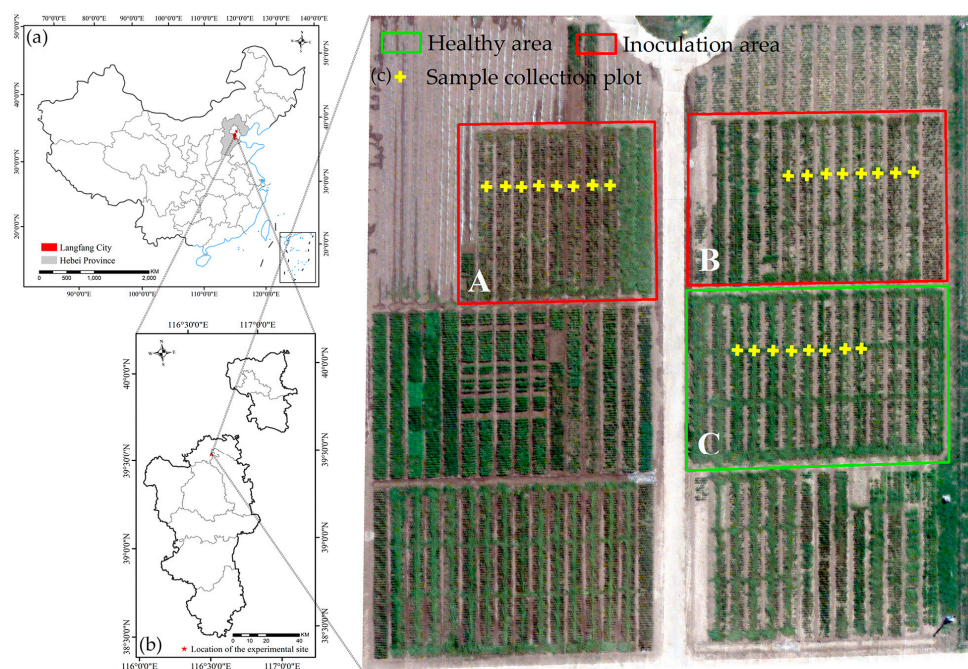

Figure 1. Study area: (**a**) the location of Langfang City; (**b**) the location of the experimental site (red star); (**c**) the image of the experimental field obtained on 30 May using a UAV equipped with a hyperspectral sensor; (**A**,**B**) are the plots inoculated with yellow rust, and (**C**) is the healthy plot; the yellow cross is the location of the sampling point.

2.2. Data Acquisition and Processing

2.2.1. Field Data Acquisition

During the critical growth period of wheat, we conducted six UAV-based hyperspectral observation experiments on 25 April, 4 May, 11 May, 18 May, 24 May, and 30 May, corresponding to 7, 16, 23, 30, 36, and 42 days post-inoculation (DPI), respectively. Figure 2 shows the development of wheat yellow rust at different infection periods. A total of 24 samples were obtained each time including eight samples obtained in the healthy plot and 16 samples obtained in the two inoculated plots. We obtained a total of 144 samples in the six experiments including 57 healthy samples and 87 yellow rust-infected samples. The severity of wheat yellow rust was described by the disease index (DI). Forty wheat plants were randomly selected from each plot with 1 m^2, and the first and second wheat leaves from the top of selected plants were used to assess the disease severity. A total of 80 leaves was selected to calculate the DI of each plot. According to the National Rules for the Investigation and Forecasting of Crop Diseases (GB/T 15795-2011) [6], the disease incidences of leaves were divided into nine categories (0%, 1%, 10%, 20%, 30%, 45%, 60%, 80%, and 100%), where 0% is healthy and 1% is disease level 1, 10% is disease level 2 . . . . . . 100% is disease level 8. The assessment of the incidence level of yellow rust was carried out immediately after the UAV had acquired the images and was performed by the same person under the guidance and supervision of a professional. The equation of the DI calculation is as follows [44]:

$$DI = \frac{\sum xf}{n\sum f} \times 100 \tag{1}$$

where x is the value of the incidence level; n is the value of the highest disease severity gradient; and f is the number of leaves for each degree of disease severity.

Figure 2. Examples of the development of yellow rust during different infection periods.

2.2.2. Unmanned Aerial Vehicle (UAV) Hyperspectral Image Acquisition

A UAV system (S1000) equipped with a hyperspectral imaging sensor (UHD 185) (Figure 3) was employed to acquire the images of wheat. The UAV hyperspectral imaging system consisted of four parts including a six-rotor electric UAV system (DJI Innovations, Shenzhen, China), a UHD 185 hyperspectral data acquisition system (Cubert GmbH, Ulm, Baden-Württemberg, Germany), a three-axis stabilized platform, and a data processing system. The UHD 185 hyperspectral imaging sensor had two charge-coupled device (CCD) detectors with a focal length of 23 mm and a pixel size of 6.45 μm [45]. The available spectral range of the UHD 185 sensor was 450–950 nm, and the spectral resolution was approximately 4 nm. The UHD 185 requires radiometric calibration before the flight and the lens exposure time is automatically matched. The flying height of the UAV was 30 m, the flying speed was 4 m/s, the forward overlap was about 80%, and the lateral overlap was about 60%. At a flying altitude of 30 m, we obtained hyperspectral images with a spatial resolution of 1.2 cm and a spectral resolution of 4 nm. The UAV hyperspectral data acquisition required clear weather with no wind or low wind speed. The image acquisition period in this study was from 11:00 a.m. to 13:00 p.m.

Figure 3. Unmanned aerial vehicle (UAV) hyperspectral imaging system.

2.2.3. UAV Hyperspectral Image Processing

Image fusion and mosaicking were performed after obtaining the UAV hyperspectral images. The Cubert–Pilot software (Cubert GmbH, Ulm, Baden-Württemberg, Germany) was used for image fusion of the hyperspectral data and the corresponding panchromatic image. Agisoft PhotoScan (Agisoft, St. Petersburg, Russia) was employed to image mosaicking. The original hyperspectral images were resampled to coarser resolutions to assess the effect of the spatial resolution on the monitoring accuracy of wheat yellow rust from UAV hyperspectral images. We resampled the original images (1.2 cm resolution) to generate new images (3, 5, 7,

10, 15, 20 cm resolution) using the nearest-neighbor algorithm. The reason for choosing these particular resolutions was that they are representative of most UAV images for monitoring the health status of crops [42,46]. Figure 4 shows an example of the UAV hyperspectral images with different spatial resolutions, which was part of area A in the image obtained on 25 April.
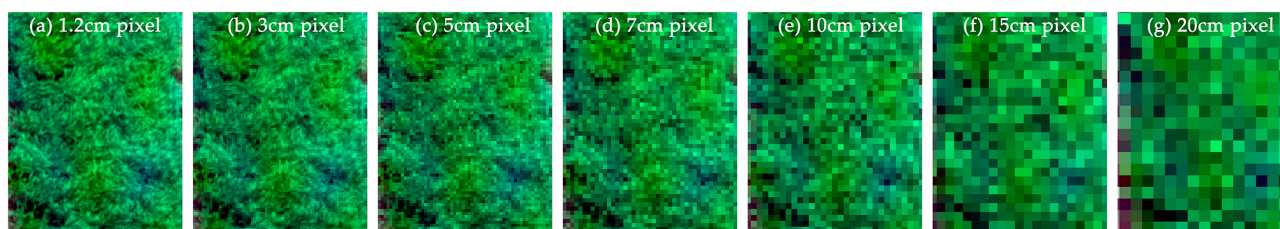

Figure 4. Example of UAV hyperspectral images with different spatial resolution. (**a**) 1.2 cm, (**b**) 3 cm, (**c**) 5 cm, (**d**) 7 cm, (**e**) 10 cm, (**f**) 15 cm, and (**g**) 20 cm.

The ground objects in the UAV images included wheat plants and soil. In this study, the NDVI [47] threshold method was used to extract wheat pixels from the images with a 1.2 cm spatial resolution [48]. The process of this method is as follows. First, set the optimal NDVI threshold. Generally, the NDVI range of vegetation was 0.3–1.0. After many attempts, we found that the NDVI threshold of 0.42 could accurately separate wheat pixels from background pixels. Second, NDVI larger than 0.42 was made into a mask file for extracting wheat pixels. Finally, we used the mask file to crop the original images to obtain the images containing only wheat pixels. For the consistency of the wheat pixels of the images with different spatial resolutions, the mask file made by the NDVI threshold of the original image (1.2 cm) was used to extract the wheat pixels of images at other spatial resolutions. The hyperspectral images containing only wheat plant pixels were used for subsequent processing and analysis.

2.3. Methods

The purpose of the image analysis was to determine which period and spatial scale provided the optimal accuracy for yellow rust identification. The process consisted of three steps: (1) extracting and selecting the VIs and TFs; (2) using partial least square regression (PLSR) to build the monitoring model of yellow rust; and (3) assessing the impact of different spatial resolutions on the monitoring accuracy.

2.3.1. Vegetation Index Extraction

Yellow rust causes abnormal fluctuations in the pigment, water content, and cell structure inside the leaves [49,50]. Therefore, we selected 15 VIs related to crop growth that were used in previous studies to evaluate their ability for monitoring wheat yellow rust. These VIs included the structural independent pigment index (SIPI), PRI, transformed chlorophyll absorption in reflectance index (TCARI), NDVI, normalized pigment chlorophyll index (NPCI), plant senescence reflectance index (PSRI), physiological reflectance index (PhRI), ARI, modified simple ratio (MSR), ratio vegetation structure index (RVSI), modified chlorophyll absorption reflectance index (MCARI), yellow rust index (YRI), greenness index (GI), triangular vegetation index (TVI), and nitrogen reflectance index (NRI). Table 1 shows the details of the VIs.

Table 1. Vegetation indices used for monitoring wheat yellow rust in this study.

VIs.	Equations	Application	Crop	Reference	Publication
SIPI	$(R_{800} - R_{445})/(R_{800} - R_{680})$	Biomass estimation and yield prediction	Potato	[51]	ISPRS Journal of Photogrammetry and Remote Sensing
PRI	$(R_{570} - R_{531})/(R_{570} + R_{531})$	Photosynthetic efficiency	Sunflower	[52]	Remote sensing of Environment
NPCI	$(R_{680} - R_{430})/(R_{680} + R_{430})$	Chlorophyll estimation	Vine	[53]	Remote sensing of Environment
MSR	$(R_{800}/R_{670} - 1)/sqrt(R_{800}/R_{670} + 1)$	Powdery mildew detection	Wheat	[18]	Computers and Electronics in Agriculture
RVSI	$((R_{712} + R_{752})/2) - R_{732}$	Target spot detection	Tomato	[33]	Precision Agriculture
YRI	$(R_{730} - R_{419})/(R_{730} + R_{419}) - 0.5R_{736}$	Yellow rust detection	Wheat	[54]	IEEE J-STARS
GI	R_{554}/R_{677}	Leaf rust detection	Wheat	[49]	Remote sensing
PhRI	$(R_{550} - R_{531})/(R_{550} + R_{531})$	Chlorophyll estimation	Corn	[55]	Remote sensing of Environment
ARI	$(R_{550})^{-1} - (R_{700})^{-1}$	Anthocyanin estimation	Norway maple	[56]	Photochemistry and Photobiology
PSRI	$(R_{680} - R_{500})/R_{750}$	Pigment estimation	Potato	[57]	Physiologia Plantarum
NRI	$(R_{570} - R_{670})/(R_{570} + R_{670})$	Nitrogen status evaluation	Wheat	[58]	Crop science
TCARI	$3((R_{700} - R_{675}) - 0.2(R_{700} - R_{500})/(R_{700}/R_{670}))$	Chlorophyll estimation	Corn	[59]	Remote sensing of Environment
TVI	$0.5 * (120(R_{750} - R_{550}) - 200(R_{670} - R_{550}))$	Laurel wilt detection	Avocado	[36]	Remote sensing of Environment
NDVI	$(R_{830} - R_{675})/(R_{830} + R_{675})$	Diseases detection	Sugar beet	[22]	Remote sensing of Environment
MCARI	$((R_{701} - R_{671}) - 0.2(R_{701} - R_{549}))/(R_{701}/R_{671})$	LAI and chlorophyll estimation	Corn	[60]	European Journal of Agronomy

2.3.2. Texture Feature Extraction

When crops are infected by diseases, changes occur in the pigment, water content, etc. as well as the shape, color, and texture of the leaves [25]. Therefore, texture is an important feature for monitoring wheat diseases. When insufficient spectral features are available to monitor diseases, TFs play an important role in improving the accuracy of disease recognition. Image texture refers to the gray-level distribution of pixels and their neighborhood [61]. Many methods have been used to define TFs including statistical, geometric, signal processing, and structural analysis methods and models [62]. The gray-level co-occurrence matrix (GLCM), a statistical method, is a proven and effective method with strong adaptability and robustness [63–66]. Therefore, the GLCM was used to extract the TFs. Eight frequently used TFs were employed to monitor yellow rust in this study. These TFs included the following features: Mean (MEA), which reflects the average grey level of all pixels in the matrix; Variance (VAR), which describes the dispersion of the values around the mean; Homogeneity (HOM), which indicates the uniformity of the matrix; Contrast (CON), which represents the local variation in the matrix; Dissimilarity (DIS), which reflects the difference in the grayscale; Entropy (ENT), which expresses the level of disorder in the matrix; Second Moment (SEC), which represents the uniformity of the grayscale; and Correlation (COR), which reflects a measurement of image linearity among the pixels [67]. The calculation equations of the TFs based on the GLCM are listed in Table 2.

Table 2. The equation of texture used in this study.

Texture	Equation
Mean, MEA	$MEA = \sum\limits_{i,j=1}^{G} iP(i,j)$
Variance, VAR	$VAR = \sum\limits_{i=1}^{G} \sum\limits_{j=1}^{G} (i-u)^2 P(i,j)$
Homogeneity, HOM	$HOM = \sum\limits_{i=1}^{G} \sum\limits_{j=1}^{G} \frac{P(i,j)}{1+(i-j)^2}$
Contrast, CON	$CON = \sum\limits_{i=1}^{G} \sum\limits_{j=1}^{G} (i-j)^2 P(i,j)$
Dissimilarity, DIS	$DIS = \sum\limits_{i=1}^{G} \sum\limits_{j=1}^{G} P(i,j)|i-j|$
Entropy, ENT	$ENT = -\sum\limits_{i=1}^{G} \sum\limits_{j=1}^{G} P(i,j)\log P(i,j)$
Second moment, SEC	$SEC = \sum\limits_{i=1}^{G} \sum\limits_{j=1}^{G} P^2(i,j)$
Correlation, COR	$COR = \sum\limits_{i=1}^{G} \sum\limits_{j=1}^{G} \frac{(i-MEA_j)(j-MEA_j)P(i,j)}{\sqrt{VAR_i}\sqrt{VAR_j}}$

Note: *i* and *j* are the row and column number of images, respectively; *P* (*i, j*) is the relative frequency of two neighboring pixels.

The TFs were extracted from the images transformed by principal component analysis (PCA) [68–70]. Extracting TFs from all bands of the original images will cause a lot of data redundancy, which has adverse effects on model accuracy. Data redundancy can be effectively reduced by converting the original image (125 bands) into several principal component (PC) images containing most of the information through PCA. In this study, PCA was completed using the PCA calculation module in the ENVI 5.1 software. The first three PC images including the first PC image (PC1), the second PC image (PC2), and the third PC image (PC3), which contained more than 96% of the cumulative variance, were used to extract the TFs. In addition, the relative distance measured in pixel numbers (d) in the GLCM was set to 1 (d = 1), and the relative orientation (θ) was the average value of four directions (θ = 0°, 45°, 90°, and 135°) [71,72]. The calculation of the TFs was conducted in MATLAB 2016a. The TFs of the samples were extracted by setting the regions of interest (ROI). First, the texture values of the whole image were calculated; then the 50 × 50 pixels regions of interest (ROI) at the sampling point were defined manually; Finally, texture values were extracted within the ROI, and the average value of the pixels in each ROI was calculated to represent the texture feature of one sample. In addition, it should be noted that the 50 × 50 pixel ROI were set in the original image (1.2 cm). For images of different spatial resolutions, we set the ROI corresponding to the size of the ROI in the original image to extract the texture features. The vegetation indices of each sample point were extracted by the same method.

2.3.3. Features Selection

Correlation analysis was used to find features (VIs and TFs) that were sensitive to the wheat yellow rust. For the relationship between DI of yellow rust and TFs, VIs were quantified by correlation coefficient (r). These features may have different sensitivities to yellow rust at different DPI. According to the disease development, we divided the data obtained in the six periods into three categories including the early infection stages (seven and 16 DPI), mid-infection stages (23 and 30 DPI), and late infection stages (36 and 42 DPI). The criteria for the selection of the sensitive features were that the feature and DI were significantly correlated in the three stages, and the average value of the correlation coefficients in the three stages was relatively large. In addition, we used the features extracted from the original images (1.2 cm resolution) to quantify the relationship with the DI of yellow rust.

2.3.4. Severity Estimation Model Based on Partial Least Squares Regression

PLSR was used to build the monitoring model of wheat yellow rust. PLSR has been previously applied for crop growth monitoring and physiological and chemical parameter estimation [18,46]. PLSR is a classic modeling method that includes the characteristics of three methods: PCA, canonical correlation analysis, and multiple linear regression analysis. In PLSR, the latent structure of the variables is determined using the component projection, which projects the predictor variables and the observed variables into a new space [73]. The original variables with high data redundancy are thus transformed into a few variables by selecting the optimal latent variables [51]. PLSR can be expressed as a linear model describing the relationship between the predictor variables and the observed variables. The expression is as follows [74]:

$$Y = \beta_0 + \beta_1 X_1 + \beta_2 X_2 + \beta_3 X_3 + \ldots + \beta_n X_n \tag{2}$$

where β_0 is the intercept; β_n are the regression coefficients; X_n are the independent variables; and n is the number of independent variables. In this study, the independent variables were the VIs, TFs, and their combination; the dependent variable was the DI of wheat yellow rust.

2.3.5. Accuracy Assessment

The coefficient of determination (R^2) and relative root mean square error (RRMSE) were used to assess the performances of the PLSR models based on different features at different spatial scales. The RRMSE is the RMSE divided by the mean of the observations. The equation of the RRMSE is [75]:

$$\text{RRMSE} = \frac{100}{\overline{Q_i}} \sqrt{\frac{1}{n} \sum_{i=1}^{n} (P_i - Q_i)^2} \tag{3}$$

where P_i and Q_i are the estimated and measured values, respectively. $\overline{Q_i}$ is the average of the measured values, and n is the number of samples. In addition, a leave-one-out cross-validation (LOOCV) approach was employed for model training and validation. This approach uses one sample for verification and $k-1$ samples for model training; k rotation was performed. The average accuracy of obtained for k times was taken as the final accuracy. The advantage of LOOCV is that almost all samples in each round are used to train the model, which can minimize overfitting and allow a more accurate and reliable assessment of model prediction. LOOCV was proven to be effective and is widely used in crop disease monitoring modeling and crop parameter inversion modeling [2,18,23,75–77]. This process was performed in MATLAB 2016 (The Math Works, Inc., Natick, MA, USA).

3. Results

3.1. Spectral Response of Wheat Yellow Rust at Different Inoculation Stages

The spectral reflectance was extracted from the 1.2 cm spatial resolution images to characterize the spectral response of wheat yellow rust at different infection periods. Figure 5 shows the canopy average spectral reflectance curves of healthy and diseased wheat in different inoculation periods (7 DPI, 16 DPI, 23 DPI, 30 DPI, 36 DPI, and 42 DPI). It can be seen from Figure 5a,b that the shape of the canopy spectral reflectance curves of healthy and yellow rust-infected wheat were similar. In the visible light region (450–680 nm), the reflectance of the wheat canopy was affected by various pigments, resulting in relatively low values. The reflectance increased rapidly in the red-edge region (680–740 nm) and the reflectance was highest in the near-infrared region (740–950 nm). In addition, with an increase in the DPI, the canopy reflectance in the near-infrared region first increased and then decreased. The reflectance of both healthy and infected wheat was significantly different in the near-infrared region at different inoculation stages, and the difference was more pronounced in the yellow rust-infected wheat. The canopy reflectance of the yellow

rust-infected wheat was lower than that of the healthy wheat in the near-infrared region (740–950 nm) in the six stages. Figure 5c shows the ratio of the spectral reflectance of the healthy and yellow rust-infected wheat in different inoculation periods. Significant differences were observed in the near-infrared region. In the early stages of inoculation (7 DPI and 16 DPI), the reflectance differences between the healthy samples and yellow rust-infected samples were negligible. However, as the DPI increased, the differences became more apparent, and the maximum difference was observed in the late stage of inoculation (42 DPI). As the DPI increased, the extent of damage to the wheat increased. Therefore, the difference between the healthy and diseased wheat became larger. The analysis of the spectral reflectance of the wheat canopy increased our understanding of the changes in disease severity and provided a basis for establishing the monitoring model of yellow rust.
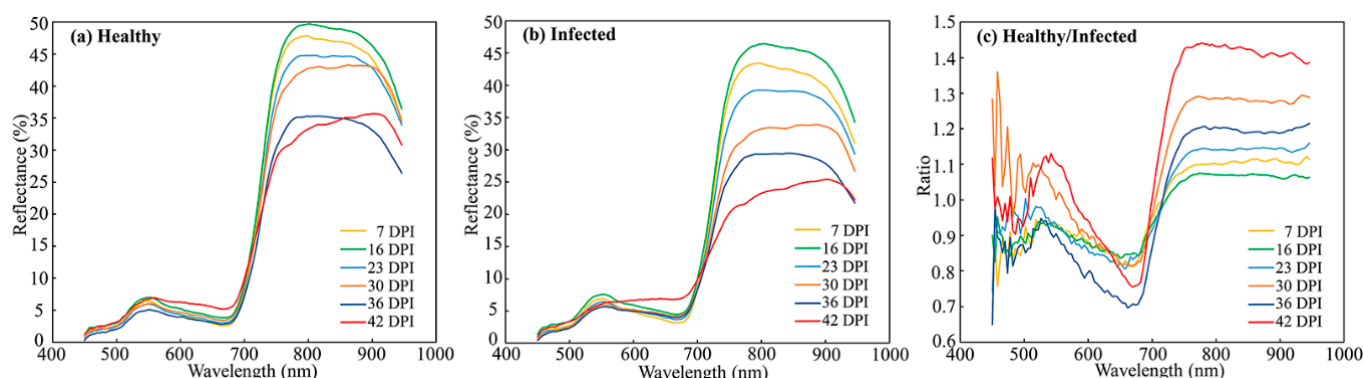

Figure 5. Canopy reflectance curves of (**a**) healthy wheat and (**b**) yellow rust-infected wheat on different inoculation dates; (**c**) the ratio of the spectral reflectance of the healthy and yellow rust-infected wheat on different inoculation dates.

3.2. Features Sensitive to Yellow Rust

Figure 6 shows the correlations between the features (VIs and TFs) and the DI. The different colors represent the different infection periods. Figure 6a shows that most VIs were strongly correlated with the DI, for instance, NDVI, SIPI, PRI, PSRI, MSR, GI, TVI, and NRI were significantly correlated with the DI at the 0.01 level ($|R|$: 0.390–0.836) in the three infection stages. Several VIs were strongly correlated with the DI in a particular period, for instance, in the late infection stage, PVSI, TCARI, and YRI were significantly correlated with the DI at the 0.01 level, with r values of 0.547, −0.782, and −0.594, respectively. Figure 6b,c shows the correlations between the TFs and the DI in different infection stages. The results showed that most TFs extracted from PC1 were significantly correlated with the DI in the mid- and late infection stages. In the early infection stage, only MEA1, VAR1, and CON1 were significantly correlated with the DI. Except for COR2, the TFs extracted from PC2 were significantly correlated with the DI in all three infection stages ($|R|$: 0.331–0.761). However, there was a very weak or no correlation between the TFs (except for MEA3 and COR3) extracted from PC3 and the DI in the three infection stages.

Too many variables cause data redundancy and processing difficulties and affect model accuracy. Therefore, we selected features that were sensitive to wheat yellow rust. According to the correlation analysis between the features and the DI, we selected features where the value of r was relatively large and passed the significance test ($p < 0.01$) in each infection period to establish the model. For the VIs, NDVI, SIPI, PRI, PSRI, MSR, GI, TVI, and NRI met the requirements. We then calculated the absolute value of the average correlation coefficient between these VIs and the DI in the three periods and sorted the values by the magnitude. Finally, the five VIs with the largest values (NDVI, SIPI, PRI, PSRI, and MSR) were selected for modeling. Only four TFs (MEA1, MEA2, VAR2, and CON2) met the requirements in the three infection stages. The selected features were input into the PLSR model to establish the monitoring model of yellow rust. The specific values

and significance levels of the correlation coefficients between the DI and VIs and TFs in the three infection stages are listed in Tables A1 and A2, respectively.
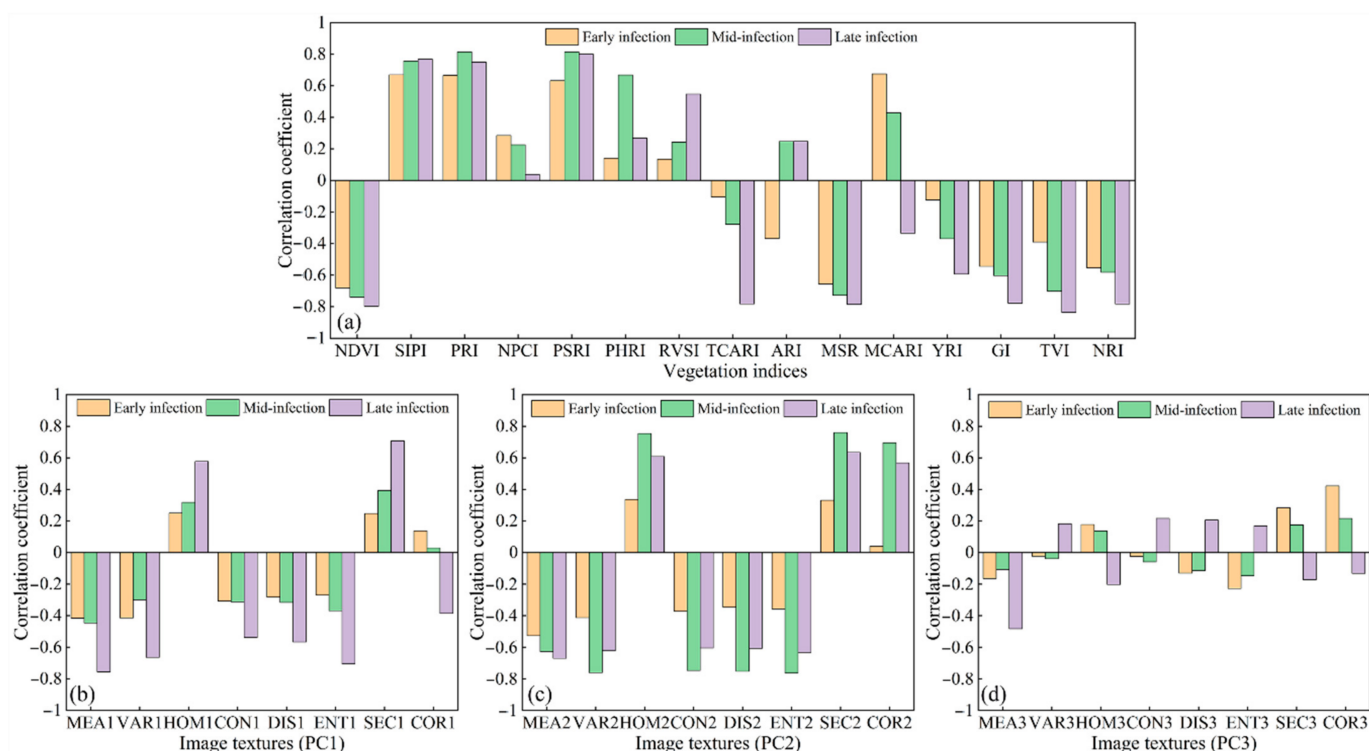

Figure 6. The correlation between the disease index (DI) and different features; (**a**) vegetation indices (VIs) and DI; (**b–d**) texture features (TFs) and DI. Note: MEA1 indicates that the mean (MEA) was extracted from the first principal component (PC) image (PC1), CON2 means that the contrast (CON) was extracted from the second PC image (PC2), and DIS3 means that the dissimilarity (DIS) was extracted from the third PC image (PC3).

3.3. Establishment and Evaluation of the Wheat Yellow Rust Monitoring Models

A suitable image spatial resolution for monitoring wheat yellow rust improves the monitoring accuracy, increases the efficiency of data processing, and reduces costs. In our study, we extracted the features from the images with seven different spatial resolutions (1.2, 3, 5, 7, 10, 15, 20 cm) in each infection period to establish the monitoring model of yellow rust and determine the optimal spatial resolution in different infection periods for monitoring yellow rust based on UAV hyperspectral images. In addition, the VI-based, TF-based, and VI-TF-based models were established to verify the performance of the combination of image features and spectral features extracted from the UAV hyperspectral images for monitoring yellow rust.

Figure 7 shows the comparison of the DI estimated accuracy of PLSR models based on different features at different infection periods and spatial resolutions. The DI estimated accuracy of the VI-based model (NDVI, SIPI, PRI, PSRI, and MSR) is presented in Figure 7a. The results showed that in the early and late infection stages, the accuracy of DI estimation at the seven spatial resolutions had a small fluctuation range (R^2 in early and late infection stages: 0.41–0.52/0.61–0.70). In the early infection stage, the highest accuracy was R^2 of 0.52 at a spatial resolution of 15 cm. In the late infection stage, the highest accuracy was an R^2 of 0.70 at a spatial resolution of 20 cm. In the mid-infection stage, except for the lowest accuracy with R^2 of 0.53 at a resolution of 7 cm, the fluctuation range at other spatial resolutions was very small (R^2: 0.69–0.75), and the highest accuracy was R^2 of 0.75 at a spatial resolution of 15 cm. In addition, we compared the accuracy at the three infection periods. The results showed that the accuracy at the mid-infection stage was the highest, except that at the spatial resolution of 7 cm. The order of accuracy of the three infection

periods was the mid-infection stage > late infection stage > early infection stage, indicating that the appropriate stage for monitoring wheat yellow rust using the VI-based model was the mid-infection stage.
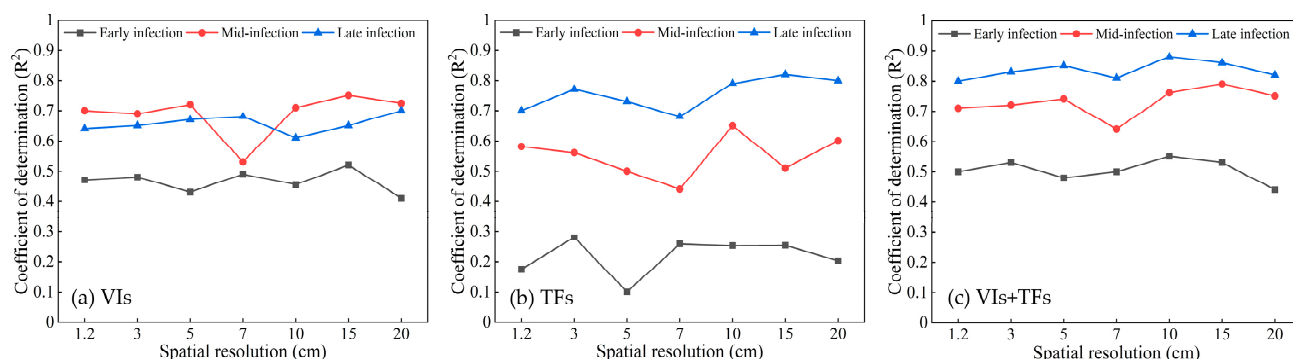

Figure 7. The monitoring accuracy (R^2) of (**a**) VI-based, (**b**) TF-based, and (**c**) VI-TF-based models at different infection stages and spatial resolutions.

For wheat yellow rust monitoring using the TF-based model (Figure 7b), different spatial scales had a greater impact on estimation accuracy. In the early infection stage, the accuracy range was R^2 of 0.1–0.28, and the highest accuracy was only R^2 of 0.28 at the spatial resolution of 3 cm. In the mid-infection stage, the estimation accuracy range was an R^2 of 0.44–0.65, of which the highest was an R^2 of 0.65 at the spatial resolution of 10 cm. In the late infection stage, the accuracy range was an R^2 of 0.68–0.82, of which the highest was an R^2 of 0.82 at the spatial resolution of 15 cm. It can be found that the estimated accuracy of the TF-based model was affected by the spatial resolution in three infection periods. In addition, the accuracy in the early infection stage was very low (the highest R^2 was only 0.28), therefore, it was not suitable to use TFs for monitoring wheat yellow rust in the early infection stage. However, the accuracies were higher in the mid- and late infection stage. In the late infection stage, we obtained the highest accuracy with an R^2 of 0.82 at the spatial resolution of 15 cm, which were the optimal stage and spatial resolution for monitoring yellow rust using the TF-based model. In addition, we compared Figure 7a,b and found that the accuracy based on VIs was higher than that based on TFs at different spatial resolutions in the early and mid-infection stages. In the late infection stage, the accuracy of the TF-based model was better than that of the VI-based model.

Figure 7c shows the monitoring accuracy of the VI-TF-based model at different spatial resolutions. The results showed that the spatial resolution had a negligible impact on the accuracy in the early and late infection stages. In the early infection stages, the range of R^2 was 0.44–0.55, and the highest accuracy was obtained at the spatial resolution of 10 cm (R^2: 0.55). In the mid-infection stage, except for the lowest accuracy at the spatial resolution of 7 cm (R^2: 0.64), the accuracy fluctuation range was relatively small (R^2: 0.64–0.79), and the highest accuracy was an R^2 of 0.79 at the spatial resolution of 15 cm. In the late infection stage, the accuracy range of R^2 was 0.80–0.88, and the highest accuracy was obtained at the spatial resolution of 10 cm (R^2: 0.55). The trend of the monitoring accuracy in different infection periods was the same for the models based on the TFs. As the infection period increased, the monitoring accuracy increased. The highest accuracy of the VI-TF-based model was obtained in the late infection stage at the spatial resolution of 10 cm. In addition, the VI-TF-based model performed better than either the VI-based or TF-based model at each spatial resolution in the three infection periods. For example, at a spatial resolution of 10 cm, the R^2 of the VI-based model in the three infection periods were 0.46, 0.71, and 0.61, those of the TF-based model were 0.25, 0.65, and 0.79, and those of the VI-TF-based model were 0.55, 0.76, and 0.88, respectively. Furthermore, a comparison of the optimal accuracy of the models at the optimal spatial resolution in each infection period (Figure 8) indicated that the VI-TF-based model provided the highest accuracy. In the early infection stage, the

monitoring accuracy of the VI-based or TF-based model was very low, especially that of the TF-based model. However, the VI-TF-based model significantly improved the accuracy. The highest R^2 of the TF-based model was only 0.25, that of the VI-based model was 0.52, and that of the VI-TF-based model was 0.55. Therefore, this result provided information to develop an effective monitoring approach for yellow rust in the early stage. The PLSR models for disease monitoring based on different features in the different infection stages at optimal spatial resolutions are shown in Table 3. The specific values of R^2 and RRMSE between the estimated DI and measured DI in the different infection stages and at different spatial resolutions using the VI-based, TF-based, and VI-TF-based models are listed in Table 3.
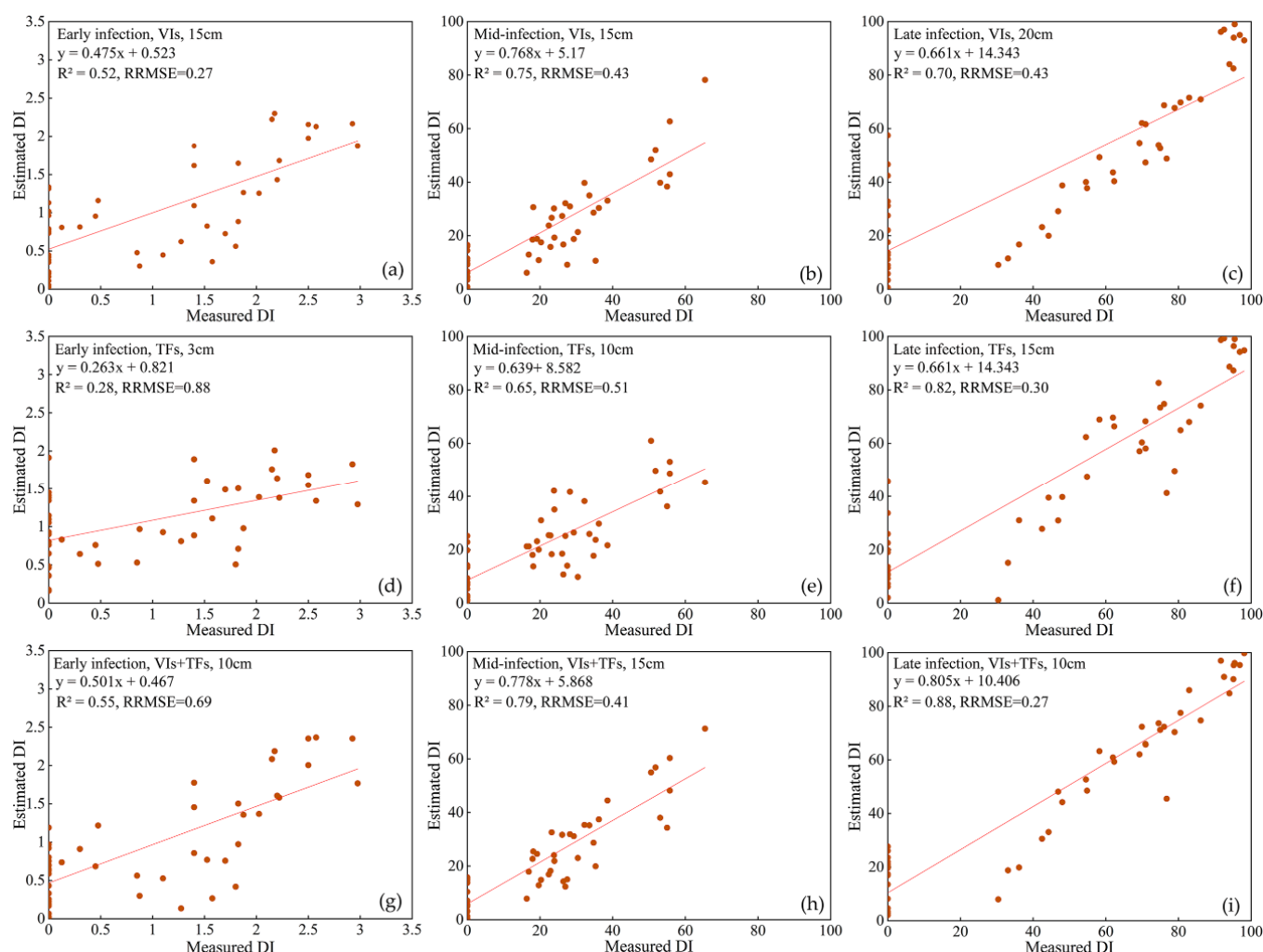

Figure 8. The scatter plots of the measured disease index (DI) versus the estimated DI of (**a–c**) the vegetation index (VI)-based model in the three infection stages at 15 cm, 15 cm, and 20 cm spatial resolution, (**d–f**) the texture feature (TF)-based model in the three infection stages at 3 cm, 10 cm, and 15 cm spatial resolution, and (**g–i**) the VI-TF-based model in the three infection stages at 10 cm, 15 cm, and 10 cm spatial resolution.

Table 3. The partial least squares regression (PLSR) models for disease monitoring based on different features in the different infection stages at optimal spatial resolutions.

Feature	Infection Stages	Spatial Resolution	PLSR-Based Model Equations
VIs	Early infection	15 cm	DI = −1.6143 − 3.9349NDVI + 6.0053SIPI + 7.173PRI + 10.3403PSRI − 0.263MSR
	Mid-infection	15 cm	DI = −391.994 + 374.044NDVI + 59.786SIPI + 338.364PRI + 759.008PSRI − 3.844MSR
	Late infection	20 cm	DI = 26.762 − 51.012NDVI + 39.463SIPI + 178.313PRI + 91.32PSRI − 8.395MSR
TFs	Early infection	3 cm	DI = 16.9718 − 0.1463MEA1 − 0.2437MEA2 − 5.8203VAR2 + 3.1486CON2
	Mid-infection	10 cm	DI = 316.811 + 0.588MEA1 − 5.671MEA2 − 32.4VAR2 + 11.707CON2
	Late infection	15 cm	DI = 479.509 + 0.54MEA1- 8.504MEA2 − 22.926VAR2 + 1.054CON2
Vis + TFs	Early infection	10 cm	DI = −4.355 − 0.008MEA1 − 0.011MEA2 + 0.094VAR2 + 0.175CON2 −4.272NDVI + 8.729SIPI + 14.065PR + 7.918PSRI − 0.189MSR
	Mid-infection	15 cm	DI = 209.235 + 1.339MEA1 − 1.75MEA2 − 109.907VAR2 + 21.766CON2 − 41.262NDVI − 18.082SIPI + 311.905PRI − 10.207PSRI − 13.047MSR
	Late infection	10 cm	DI = −248.697 + 2.211MEA1 − 4.391MEA2 − 14.686VAR2 + 4.341CON2 + 421.597NDVI + 69 SIPI + 288.678PRI + 680.157PSRI − 5.277MSR

The VI-TF-based model with the highest monitoring accuracy in the three infection stages was used to map the yellow rust distribution. For the optimal spatial resolution, in the early and late infection stages, the VI-TF-based model achieved the highest accuracy at a spatial resolution of 10 cm with an R^2 of 0.55 and 0.88, respectively. In the mid-infection stage, the highest accuracy was obtained at a spatial resolution of 15 cm (R^2 = 0.79), and the monitoring accuracy was also high at a spatial resolution of 10 cm (R^2 = 0.76). The accuracy difference was very small between the models at a 10 cm and 15 cm spatial resolution. Therefore, we used the VI-TF-based model to map wheat yellow rust at the 10 cm spatial resolution in the three infection periods. According to the suggestion from the National Plant Protection Department, the DI was classified into four classes including healthy (DI ≤ 5%), slight infection (5 < DI ≤ 20%), moderate infection (20 < DI ≤ 50%), and severe infection (DI > 50%). The spatial distribution of yellow rust in the study area is shown in Figure 9. It can be seen from Figure 9 that the wheat in the inoculation plots (A and B) were seriously infected, and the location of the disease was mainly in the middle of each row in the three infection periods, which was attributed to the location of the inoculation of the pathogen. The infected area and severity increased from the early to the late infection stage, and the infected areas of wheat yellow rust in the early infection stage was very small (Figure 9a), since the wheat had only been inoculated for a short time, the disease was just beginning to develop. The diseases developed rapidly in the mid-infection period (Figure 9b) due to the pathogen accumulation in the early infection stage and suitable environmental factors. In the late infection stage, most wheat in the field was infected with yellow rust (Figure 9c). The wheat yellow rust in the healthy plot (C) was not detected in the early infection stage, and mild diseases were detected in the mid- and late infection stages. The reason may be that we implemented pesticide prevention in the healthy area, resulting in almost no yellow rust on the wheat in this area; the mild disease may have spread from the inoculation area (A and B). In addition, the monitoring model also has certain monitoring errors. The distribution and development of yellow rust in the experiment area were basically in line with the spread of yellow rust and the observations in this experiment.
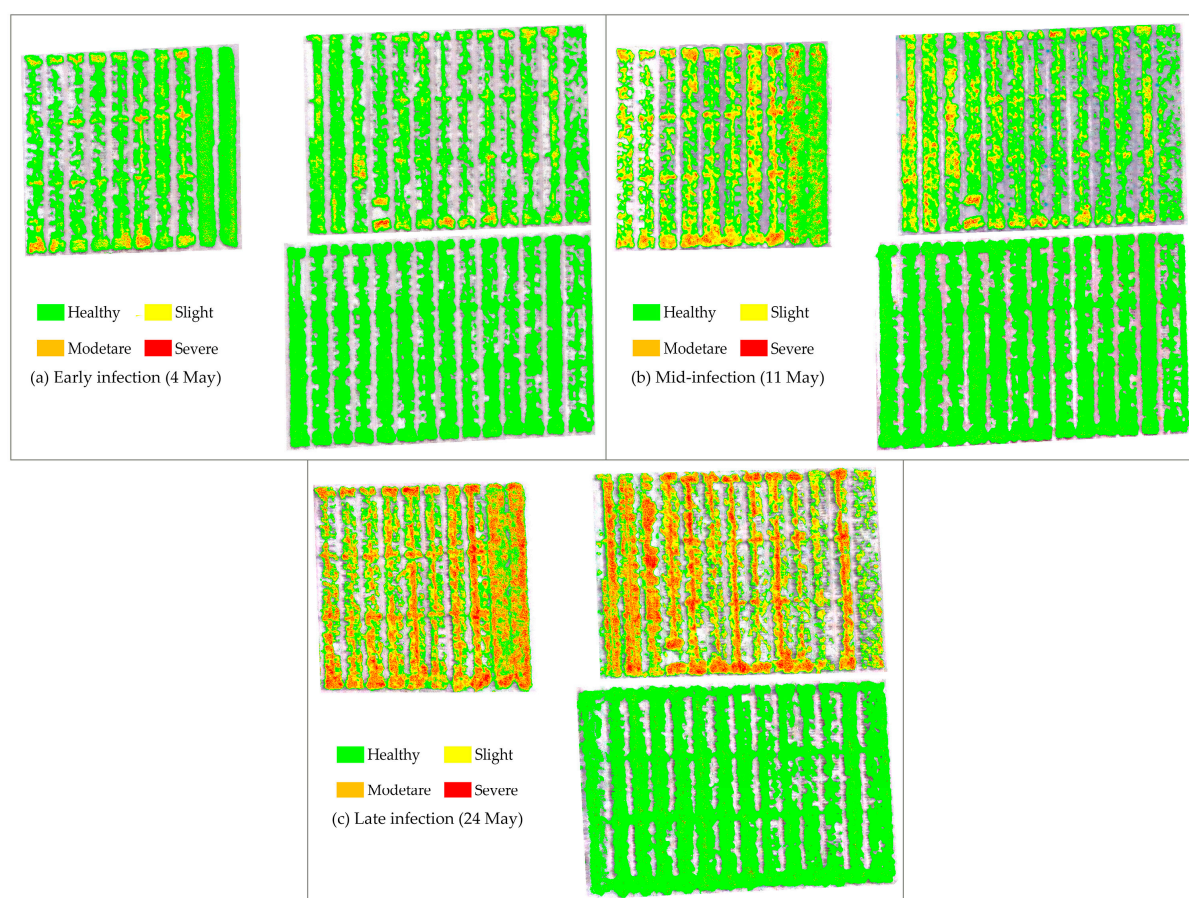
Figure 9. The spatial distribution of wheat yellow rust mapped using the VI-TF-based model in the (**a**) early infection stage (4 May), (**b**) mid-infection stage (11 May), and (**c**) late infection stage (24 May).

4. Discussion

The spectral response of crop diseases is the basis of remote sensing monitoring. Previous studies have confirmed that crops affected by diseases exhibit changes in the pigment, water content, and cell structure of the leaves, and these changes are reflected in the spectrum [78]. Changes in pigment generally cause spectral responses in the visible range, while changes in cell structure cause spectral responses in the near-infrared range. Figure 5 shows that the spectral reflectance of yellow rust-infected wheat was higher than that of healthy wheat in the visible range (450–680 nm), and lower than that of healthy wheat in the near-infrared range (720–950 nm), which may be caused by yellow rust destroying the pigment and altering the cell structure in the leaves. In addition, when wheat is infected by yellow rust, bright yellow spore piles form on the surface of the leaves, which not only affect the spectrum by invading the inside of the leaf and destroying the physiological parameters, but also cause the change in the spectrum through the change in the surface color. These results were consistent with those of Guo et al. [18]. Figure 5 also shows that the spectral reflectance of healthy and yellow rust-infected wheat in the near-infrared range first increased and then decreased with the increase in inoculation time. For healthy wheat, this may be caused by the growth and development of wheat; for diseased wheat, in addition to the effects of wheat growth and development, it may also be caused by the continuous development of diseases over time. The severity of the disease gradually increased over time, and the effects became visible; thus, the spectral reflectance changes were more significant in the later stages. Zheng et al. [2] also observed similar results. In this study, NDVI, SIPI, PRI, PSRI, and MSR were selected to monitor yellow rust. Previous studies have concluded that these indices are closely related to photosynthetic efficiency [52,79], the ratio of carotenoids to chlorophyll, and LAI. Yellow rust destroys pigments and affects

the photosynthetic efficiency as well as the LAI at the canopy scale. Therefore, the selected VIs were sensitive to yellow rust.

Based on PLSR, the yellow rust monitoring models were established with different features in different infection periods. The results showed that the VI-TF-based models were better than the VI-based or TF-based models. For example, in the late infection stage, the accuracy of the VI-TF-based model was $R^2 = 0.88$ at a spatial resolution of 10 cm, which was 0.09 and 0.27 higher than that of the TF-based and VI -based models, respectively. The VI-based model only reflected the changes in pigment and cell structure inside the leaves caused by yellow rust, while the TF-based model only reflected the changes in color and shape outside the leaves. The advantage of the TF-VI-based model is that it combines VIs (NDVI, SIPI, PRI, PSRI and MSR) and TFs (MEA1, MEA2, VAR2 and CON2), which can reflect both the internal and external changes of leaves caused by yellow rust. These results were consistent with our previous research, which was conducted on the leaf scale [25]. This study was the first to demonstrate the effectiveness of monitoring yellow rust using the combination of VIs and TFs at the field scale. In addition, the results showed that the accuracy of the VI-based model was higher than that of the TF-based model in the early and mid-infection stages and lower than that of the TF-based model in the late infection stage. For example, at a spatial resolution of 10 cm, the accuracies of the VI-based models were R^2 of 0.46, 0.71, and 0.61 in the three infection stages, which were 0.21 and 0.06 higher than TF-based models in early and mid-infection stages, respectively, and which was 0.18 lower than the TF-based model in the late infection stage. Disease symptom development may have caused this situation. In the early and mid-infection, yellow rust is asymptomatic or mild, resulting in less information on the external changes being captured by the TFs, while VIs can capture the changes inside the leaves at this time. When the symptoms of yellow rust become obvious in the late infection stage, TFs, which can represent more disease information, have a great advantage over VIs.

In this study, we also evaluated the impact of the spatial resolution on the monitoring accuracy of yellow rust. The results showed that the spatial resolution had a negligible effect on the monitoring accuracy of the VI-based models (Figure 7). The reason may be that the nearest-neighbor algorithm was used to resample the images to change the spatial resolution. Theoretically, the reflectance values of the image pixels will not change after resampling [36]. VIs are converted from spectral bands, so their values will not change. This result was consistent with that of Zhang et al. [42]. The impact of the spatial resolution on the monitoring accuracy of the TF-based models was greater than that of the VI-based models (Figure 7). The texture was calculated based on the size of the pixels and the neighborhood relationship [80]. The pixel size and position may have changed after resampling, resulting in textural changes. Therefore, the accuracy of the TF-based models was significantly affected by spatial resolution. Based on the VI-TF model, the optimal spatial resolution for monitoring wheat yellow rust at the three infection periods was about 10 cm. The reason for obtaining a higher accuracy at the spatial resolution of 10 cm may be related to the size of the wheat plants. Dash et al. [41] obtained similar results when using UAV multispectral images with different spatial resolutions to monitor the occurrence of forest diseases. The optimal spatial resolution for monitoring forest diseases was 1 m, which was similar to the radius of the trees (1.52 m). Therefore, the optimal spatial resolution may not necessarily be the highest resolution, but may depend on the monitoring object.

Crop disease monitoring relies largely on the use of appropriate platforms, sensors, and analysis methods to obtain the optimal spectral, spatial, and temporal features of the diseases. For the monitoring of wheat diseases, near-surface spectral measurement technology is relatively mature including non-imaging sensors (e.g., spectrometers (ASD)) and imaging sensors (e.g., hyperspectral sensors (Headwall Photonics)), which enable remote sensing monitoring of wheat diseases. However, these technologies cannot be applied to the field or larger scales to prevent and monitor diseases. Satellite technology can be used for crop disease monitoring on a large scale, however, due to the limitation of the spectral and time characteristics, current satellite technology has certain limitations for

the field-scale monitoring of crop diseases. In addition, satellite sensors are also affected by external factors such as weather and clouds. UAV technology overcomes these limitations with the advantages of low cost and flexibility, providing a new strategy for monitoring crop diseases at the field scale. We successfully acquired hyperspectral images using the DJI UAV equipped with UHD 185 sensors, extracted the optimal features (the combination of VIs and TFs), and selected the optimal spatial resolution for wheat yellow rust monitoring. However, we encountered several limitations. First, we resampled the original images to obtain images with different spatial resolutions to evaluate the impact of different spatial resolutions on the monitoring accuracy. In the future, we will fly the UAV at different altitudes to obtain images at different spatial resolutions rather than simulate the image resolution. Second, in the case of a small sample size, the LOOCV was used to model training and validation. To reduce the impact of spatial autocorrelation of the sample on the modeling accuracy, we will collect more samples, and use samples from different fields to train and verify the model separately. In addition, the proposed method generally did not have high monitoring accuracy in the early stages of disease development, which is the key stage for disease prevention. Therefore, accurate monitoring and effective prevention measures in the early infection stage are essential to minimize the damage caused by the disease. In a follow-up study, we will investigate different methods (e.g., establishing a new spectral index sensitive to yellow rust) to monitor wheat yellow rust in the early infection stage based on UAV images. Furthermore, UAV multispectral images have also been used for disease monitoring and have the advantages of low cost and convenient data acquisition and processing. In the future, we will analyze the use of multispectral images for monitoring yellow rust at the field scale.

5. Conclusions

In this study, UAV hyperspectral images were used to monitor wheat yellow rust at the field scale. We used different features (VIs, TFs, and their combination) to establish PLSR monitoring models of wheat yellow rust in the early, mid-, and late infection stages. We evaluated the impact of different image spatial resolutions (1.2 cm, 3 cm, 5 cm, 7 cm, 10 cm, 15 cm, and 20 cm) on monitoring accuracy. The following conclusions were obtained. (1) The VI-based model provided the highest monitoring accuracy in the mid-infection stage, and the TF-based model yielded the highest monitoring accuracy in the late infection stage. However, the TF-based model was unsuitable to monitor yellow rust in the early infection stage, the highest monitoring accuracy was only an R^2 of 0.28. (2) The VI-TF-based model provided higher accuracy than the VI-based or TF-based model in the three infection periods, and provided the highest accuracy in the late infection stage ($R^2 = 0.88$). In addition, the monitoring accuracy in the early infection stage was significantly improved by using the VI-TF-based model; thus, this model is suitable for the early detection of diseases. (3) The spatial resolution had a negligible influence on the monitoring accuracy of the VI-based models and a greater influence on the TF-based models. The optimal spatial resolution for the VI-TF-based model for monitoring yellow rust was 10 cm. In subsequent studies, we will focus on the precise monitoring of wheat yellow rust in the early infection stage to provide a basis for disease prevention.

Institutional Review Board Statement: This study not involving humans.

Informed Consent Statement: This study not involving humans.

Data Availability Statement: Data sharing is not applicable to this article.

Appendix A

Table A1. The correlation coefficients between the DI and VIs in the three infection stages.

VIs	Early Infection	Mid-Infection	Late Infection
NDVI	−0.681 **	−0.739 **	−0.797 **
SIPI	0.669 **	0.757 **	0.768 **
PRI	0.665 **	0.814 **	0.750 **
NPCI	0.284	0.226	0.038
PSRI	0.632 **	0.814 **	0.800 **
PhRI	0.140	0.668 **	0.268
RVSI	0.135	0.243	0.547 **
TCARI	−0.104	−0.277	−0.782 **
ARI	−0.368 *	0.247	0.247
MSR	−0.656 **	−0.728 **	−0.785 **
MCARI	0.675 **	0.428 **	−0.334 *
YRI	−0.123	−0.370 **	−0.594 **
GI	−0.544 **	−0.603 **	−0.777 **
TVI	−0.390 **	−0.702 **	−0.836 **
NRI	−0.554 **	−0.582 **	−0.783 **

Note: ** indicates that the correlation was significant at the 0.01 level; * indicates that the correlation was significant at the 0.05 level. The features highlighted in gray are related to the DI at the 0.01 level in all three infection periods.

Table A2. The correlation coefficients between the DI and TFs in the three infection stages.

TFs	Early Infection	Mid-Infection	Late Infection
MEA1	−0.417 **	−0.446 **	−0.755 **
VAR1	−0.414 **	−0.299 *	−0.664 **
HOM1	0.249	0.318 *	0.577 **
CON1	−0.308 *	−0.312 *	−0.538 **
DIS1	−0.283	−0.316 *	−0.567 **
ENT1	−0.270	−0.369 **	−0.706 **
SEC1	0.247	0.393 **	0.707 **
COR1	0.137	0.029	−0.386 **
MEA2	−0.527 **	−0.627 **	−0.670 **
VAR2	−0.413 **	−0.761 **	−0.623 **
HOM2	0.336 *	0.754 **	0.608 **
CON2	−0.372 **	−0.747 **	−0.605 **
DIS2	−0.346 *	−0.753 **	−0.607 **
ENT2	−0.357 *	−0.764 **	−0.633 **
SEC2	0.331 *	0.760 **	0.634 **
COR2	0.039	0.695 **	0.568 **
MEA3	−0.164	−0.107	−0.483 **
VAR3	−0.023	−0.040	0.182
HOM3	0.177	0.137	−0.202
CON3	−0.024	−0.060	0.216
DIS3	−0.131	−0.115	0.205
ENT3	−0.228	−0.147	0.169
SEC3	0.283	0.175	−0.172
COR3	0.422 **	0.215	−0.132

Note: ** indicates that the correlation was significant at the 0.01 level; * indicates that the correlation was significant at the 0.05 level. The features highlighted in gray are related to the DI at the 0.01 level in all three infection periods.

Table 3. The coefficients of determination (R^2) and RRMSE between the estimated DI and measured DI in the different infection stages at different spatial resolutions for the VI-based, TF-based, and VI-TF-based models.

Feature	Infection Stages	R^2/RRMSE						
		1.2 cm	3 cm	5 cm	7 cm	10 cm	15 cm	20 cm
VIs	Early infection	0.47/0.755	0.48/0.757	0.43/0.758	0.49/0.756	0.46/0.765	0.52/0.716	0.41/0.793
	Mid-infection	0.70/0.472	0.69/0.470	0.72/0.469	0.53/0.605	0.71/0.469	0.75/0.425	0.72/0.457
	Late infection	0.64/0.469	0.65/0.468	0.67/0.467	0.68/0.465	0.61/0.467	0.65/0.467	0.70/0.428
TFs	Early infection	0.18/0.942	0.28/0.880	0.10/0.984	0.26/0.893	0.25/0.896	0.25/0.896	0.20/0.926
	Mid-infection	0.58/0.566	0.56/0.566	0.50/0.563	0.44/0.585	0.65/0.513	0.51/0.608	0.60/0.574
	Late infection	0.70/0.388	0.77/0.380	0.73/0.365	0.68/0.367	0.79/0.359	0.82/0.332	0.80/0.352
Vis + TFs	Early infection	0.50/0.694	0.53/0.748	0.48/0.776	0.50/0.784	0.55/0.694	0.53/0.768	0.44/0.812
	Mid-infection	0.71/0.464	0.72/0.460	0.74/0.471	0.64/0.518	0.76/0.415	0.79/0.406	0.75/0.456
	Late infection	0.80/0.332	0.83/0.320	0.85/0.301	0.81/0.285	0.88/0.266	0.86/0.319	0.82/0.311

Note: The numbers before and after "/" are the R^2 and RRMSE, respectively. The values in the gray box are the highest values of each feature in the different infection periods and spatial resolutions.

References

1. Han, J.; Zhang, Z.; Cao, J.; Luo, Y.; Zhang, L.; Li, Z.; Zhang, J. Prediction of Winter Wheat Yield Based on Multi-Source Data and Machine Learning in China. *Remote Sens.* **2020**, *12*, 236. [CrossRef]
2. Zheng, Q.; Huang, W.; Cui, X.; Dong, Y.; Shi, Y.; Ma, H.; Liu, L. Identification of Wheat Yellow Rust Using Optimal Three-Band Spectral Indices in Different Growth Stages. *Sensors* **2018**, *19*, 35. [CrossRef] [PubMed]
3. Ma, H.; Huang, W.; Jing, Y.; Pignatti, S.; Laneve, G.; Dong, Y.; Ye, H.; Liu, L.; Guo, A.; Jiang, J. Identification of Fusarium Head Blight in Winter Wheat Ears Using Continuous Wavelet Analysis. *Sensors* **2020**, *20*, 20. [CrossRef] [PubMed]
4. Moshou, D.; Bravo, C.; West, J.; Wahlen, S.; McCartney, A.; Ramon, H. Automatic detection of 'yellow rust' in wheat using reflectance measurements and neural networks. *Comput. Electron. Agric.* **2004**, *44*, 173–188. [CrossRef]
5. Chen, X. Epidemiology and control of stripe rust [*Puccinia striiformis* f. sp. *tritici*] on wheat. *Can. J. Plant. Pathol.* **2005**, *27*, 314–337. [CrossRef]
6. Zheng, Q.; Huang, W.; Cui, X.; Shi, Y.; Liu, L. New spectral index for detecting wheat yellow rust using sentinel-2 multispectral imagery. *Sensors* **2018**, *18*, 868. [CrossRef]
7. Yu, K.; Anderegg, J.; Mikaberidze, A.; Karisto, P.; Mascher, F.; McDonald, B.A.; Walter, A.; Hund, A. Hyperspectral Canopy Sensing of Wheat Septoria Tritici Blotch Disease. *Front. Plant. Sci.* **2018**, *9*, 1195. [CrossRef]
8. He, L.; Qi, S.-L.; Duan, J.-Z.; Guo, T.-C.; Feng, W.; He, D.-X. Monitoring of Wheat Powdery Mildew Disease Severity Using Multiangle Hyperspectral Remote Sensing. *ITGRS* **2020**. [CrossRef]
9. Hatton, N.M.; Menke, E.; Sharda, A.; van der Merwe, D.; Schapaugh, W., Jr. Assessment of sudden death syndrome in soybean through multispectral broadband remote sensing aboard small unmanned aerial systems. *Comput. Electron. Agric.* **2019**, *167*, 105094. [CrossRef]
10. Chivasa, W.; Onisimo, M.; Biradar, C.M. UAV-Based Multispectral Phenotyping for Disease Resistance to Accelerate Crop Improvement under Changing Climate Conditions. *Remote Sens.* **2020**, *12*, 2445. [CrossRef]
11. Abdulridha, J.; Ehsani, R.; Abd-Elrahman, A.; Ampatzidis, Y. A remote sensing technique for detecting laurel wilt disease in avocado in presence of other biotic and abiotic stresses. *Comput. Electron. Agric.* **2019**, *156*, 549–557. [CrossRef]
12. Abdulridha, J.; Ampatzidis, Y.; Roberts, P.D.; Kakarla, S.C. Detecting powdery mildew disease in squash at different stages using UAV-based hyperspectral imaging and artificial intelligence. *Biosyst. Eng.* **2020**, *197*, 135–148. [CrossRef]
13. Awad, M.M. Forest mapping: A comparison between hyperspectral and multispectral images and technologies. *J. For. Res.* **2017**, *29*, 1395–1405. [CrossRef]
14. Yang, C.; Fernandez, C.J.; Everitt, J.H. Comparison of airborne multispectral and hyperspectral imagery for mapping cotton root rot. *Biosyst. Eng.* **2010**, *107*, 131–139. [CrossRef]
15. Mariotto, I.; Thenkabail, P.S.; Huete, A.R.; Slonecker, E.T.; Platonov, A. Hyperspectral versus multispectral crop-productivity modeling and type discrimination for the HyspIRI mission. *Remote Sens. Environ.* **2013**, *139*, 291–305. [CrossRef]
16. Yao, Z.; Lei, Y.; He, D. Early Visual Detection of Wheat Stripe Rust Using Visible/Near-Infrared Hyperspectral Imaging. *Sensors* **2019**, *19*, 952. [CrossRef] [PubMed]
17. Shi, Y.; Huang, W.; González-Moreno, P.; Luke, B.; Dong, Y.; Zheng, Q.; Ma, H.; Liu, L. Wavelet-Based Rust Spectral Feature Set (WRSFs): A Novel Spectral Feature Set Based on Continuous Wavelet Transformation for Tracking Progressive Host–Pathogen Interaction of Yellow Rust on Wheat. *Remote Sens.* **2018**, *10*, 525. [CrossRef]
18. Zhang, J.-C.; Pu, R.-L.; Wang, J.-H.; Huang, W.-J.; Yuan, L.; Luo, J.-H. Detecting powdery mildew of winter wheat using leaf level hyperspectral measurements. *Comput. Electron. Agric.* **2012**, *85*, 13–23. [CrossRef]
19. Chen, T.; Zhang, J.; Chen, Y.; Wan, S.; Zhang, L. Detection of peanut leaf spots disease using canopy hyperspectral reflectance. *Comput. Electron. Agric.* **2019**, *156*, 677–683. [CrossRef]

20. Gu, Q.; Sheng, L.; Zhang, T.; Lu, Y.; Zhang, Z.; Zheng, K.; Hu, H.; Zhou, H. Early detection of tomato spotted wilt virus infection in tobacco using the hyperspectral imaging technique and machine learning algorithms. *Comput. Electron. Agric.* **2019**, *167*, 105066. [CrossRef]

21. Yang, C.-M. Assessment of the severity of bacterial leaf blight in rice using canopy hyperspectral reflectance. *Precis. Agric.* **2010**, *11*, 61–81. [CrossRef]

22. Mahlein, A.; Rumpf, T.; Welke, P.; Dehne, H.-W.; Plumer, L.; Steiner, U.; Oerke, E.-C. Development of spectral indices for detecting and identifying plant diseases. *Remote Sens. Environ* **2013**, *128*, 21–30. [CrossRef]

23. Liu, L.; Dong, Y.; Huang, W.; Du, X.; Ren, B.; Huang, L.; Zheng, Q.; Ma, H. A Disease Index for Efficiently Detecting Wheat Fusarium Head Blight Using Sentinel-2 Multispectral Imagery. *IEEE Access* **2020**, *8*, 52181–52191. [CrossRef]

24. Pydipati, R.; Burks, T.; Lee, W.S. Identification of citrus disease using color texture features and discriminant analysis. *Comput. Electron. Agric.* **2006**, *52*, 49–59. [CrossRef]

25. Guo, A.; Huang, W.; Ye, H.; Dong, Y.; Ma, H.; Ren, Y.; Ruan, C. Identification of Wheat Yellow Rust Using Spectral and Texture Features of Hyperspectral Images. *Remote Sens.* **2020**, *12*, 1419. [CrossRef]

26. Al-Saddik, H.; Laybros, A.; Billiot, B.; Cointault, F. Using image texture and spectral reflectance analysis to detect Yellowness and Esca in grapevines at leaf-level. *Remote Sens* **2018**, *10*, 618. [CrossRef]

27. Su, J.; Liu, C.; Hu, X.; Xu, X.; Guo, L.; Chen, W.-H. Spatio-temporal monitoring of wheat yellow rust using UAV multispectral imagery. *Comput. Electron. Agric.* **2019**, *167*, 105035. [CrossRef]

28. Su, J.; Liu, C.; Coombes, M.; Hu, X.; Wang, C.; Xu, X.; Li, Q.; Guo, L.; Chen, W.-H. Wheat yellow rust monitoring by learning from multispectral UAV aerial imagery. *Comput. Electron. Agric.* **2018**, *155*, 157–166. [CrossRef]

29. Calou, V.B.C.; Teixeira, A.D.S.; Moreira, L.C.J.; Lima, C.S.; De Oliveira, J.B.; De Oliveira, M.R.R. The use of UAVs in monitoring yellow sigatoka in banana. *Biosyst. Eng.* **2020**, *193*, 115–125. [CrossRef]

30. Ye, H.; Huang, W.; Huang, S.; Cui, B.; Dong, Y.; Guo, A.; Ren, Y.; Jin, Y. Recognition of Banana Fusarium Wilt Based on UAV Remote Sensing. *Remote Sens.* **2020**, *12*, 938. [CrossRef]

31. Franceschini, M.H.D.; Bartholomeus, H.M.; Van Apeldoorn, D.F.; Suomalainen, J.; Kooistra, L. Feasibility of Unmanned Aerial Vehicle Optical Imagery for Early Detection and Severity Assessment of Late Blight in Potato. *Remote Sens.* **2019**, *11*, 224. [CrossRef]

32. Mahlein, A.-K. Plant Disease Detection by Imaging Sensors—Parallels and Specific Demands for Precision Agriculture and Plant Phenotyping. *Plant Dis.* **2016**, *100*, 241–251. [CrossRef] [PubMed]

33. Abdulridha, J.; Ampatzidis, Y.; Kakarla, S.C.; Roberts, P.D. Detection of target spot and bacterial spot diseases in tomato using UAV-based and benchtop-based hyperspectral imaging techniques. *Precis. Agric.* **2019**, *21*, 955–978. [CrossRef]

34. Abdulridha, J.; Batuman, O.; Ampatzidis, Y. UAV-based remote sensing technique to detect citrus canker disease utilizing hyperspectral imaging and machine learning. *Remote Sens.* **2019**, *11*, 1373. [CrossRef]

35. Deng, X.; Zhu, Z.; Yang, J.; Zheng, Z.; Huang, Z.; Yin, X.; Wei, S.; Lan, Y. Detection of Citrus Huanglongbing Based on Multi-Input Neural Network Model of UAV Hyperspectral Remote Sensing. *Remote Sens.* **2020**, *12*, 2678. [CrossRef]

36. De Castro, A.; Ehsani, R.; Ploetz, R.; Crane, J.; Abdulridha, J. Optimum spectral and geometric parameters for early detection of laurel wilt disease in avocado. *Remote Sens. Environ.* **2015**, *171*, 33–44. [CrossRef]

37. Ramírez-Cuesta, J.; Allen, R.; Zarco-Tejada, P.J.; Kilic, A.; Santos, C.; Lorite, I. Impact of the spatial resolution on the energy balance components on an open-canopy olive orchard. *Int. J. Appl. Earth Obs. Geoinf.* **2019**, *74*, 88–102. [CrossRef]

38. Roth, K.L.; Roberts, D.A.; Dennison, P.E.; Peterson, S.H.; Alonzo, M. The impact of spatial resolution on the classification of plant species and functional types within imaging spectrometer data. *Remote Sens. Environ.* **2015**, *171*, 45–57. [CrossRef]

39. Breunig, F.M.; Galvão, L.S.; Dalagnol, R.; Santi, A.L.; Della Flora, D.P.; Chen, S. Assessing the effect of spatial resolution on the delineation of management zones for smallholder farming in southern Brazil. *Remote Sens. Appl. Soc. Environ.* **2020**, *19*, 100325.

40. Zhou, K.; Cheng, T.; Zhu, Y.; Cao, W.; Ustin, S.L.; Zheng, H.; Yao, X.; Tian, Y. Assessing the impact of spatial resolution on the estimation of leaf nitrogen concentration over the full season of paddy rice using near-surface imaging spectroscopy data. *Front. Plant Sci.* **2018**, *9*, 964. [CrossRef]

41. Dash, J.P.; Watt, M.S.; Pearse, G.D.; Heaphy, M.; Dungey, H.S. Assessing very high resolution UAV imagery for monitoring forest health during a simulated disease outbreak. *ISPRS J. Photogramm. Remote Sens.* **2017**, *131*, 1–14. [CrossRef]

42. Zhang, J.; Wang, C.; Yang, C.; Xie, T.; Jiang, Z.; Hu, T.; Luo, Z.; Zhou, G.; Xie, J. Assessing the Effect of Real Spatial Resolution of In Situ UAV Multispectral Images on Seedling Rapeseed Growth Monitoring. *Remote Sens.* **2020**, *12*, 1207. [CrossRef]

43. Liu, M.; Yu, T.; Gu, X.; Sun, Z.; Yang, J.; Zhang, Z.; Mi, X.; Cao, W.; Li, J. The Impact of Spatial Resolution on the Classification of Vegetation Types in Highly Fragmented Planting Areas Based on Unmanned Aerial Vehicle Hyperspectral Images. *Remote Sens.* **2020**, *12*, 146. [CrossRef]

44. Huang, W.; Lamb, D.W.; Niu, Z.; Zhang, Y.; Liu, L.; Wang, J. Identification of yellow rust in wheat using in-situ spectral reflectance measurements and airborne hyperspectral imaging. *Precis. Agric.* **2007**, *8*, 187–197. [CrossRef]

45. Cubert-GmbH Hyperspectral Firefleye S185 SE. Available online: http://cubert-gmbh.de/ (accessed on 15 October 2020).

46. Yue, J.; Yang, G.; Tian, Q.; Feng, H.; Xu, K.; Zhou, C. Estimate of winter-wheat above-ground biomass based on UAV ultrahigh-ground-resolution image textures and vegetation indices. *ISPRS J. Photogramm. Remote. Sens.* **2019**, *150*, 226–244. [CrossRef]

47. Rouse, J.W., Jr.; Haas, R.H.; Schell, J.A.; Deering, D.W. Monitoring vegetation systems in the great plains with ERTS. In Proceedings of the Third Earth Resources Technology Satellite-1 Symposium, Washington, DC, USA, 10–14 December 1973; pp. 309–317.

48. Zhang, X.; Han, L.; Dong, Y.; Shi, Y.; Huang, W.; Han, L.; González-Moreno, P.; Ma, H.; Ye, H.; Sobeih, T. A Deep Learning-Based Approach for Automated Yellow Rust Disease Detection from High-Resolution Hyperspectral UAV Images. *Remote Sens.* **2019**, *11*, 1554. [CrossRef]

49. Ashourloo, D.; Mobasheri, M.R.; Huete, A. Developing two spectral disease indices for detection of wheat leaf rust (Pucciniatriticina). *Remote Sens.* **2014**, *6*, 4723–4740. [CrossRef]

50. Devadas, R.; Lamb, D.W.; Simpfendorfer, S.; Backhouse, D. Evaluating ten spectral vegetation indices for identifying rust infection in individual wheat leaves. *Precis. Agric.* **2008**, *10*, 459–470. [CrossRef]

51. Li, B.; Li, B.; Zhang, L.; Han, J.; Bian, C.; Li, G.; Xu, X.; Li-Ping, J. Above-ground biomass estimation and yield prediction in potato by using UAV-based RGB and hyperspectral imaging. *ISPRS J. Photogramm. Remote. Sens.* **2020**, *162*, 161–172. [CrossRef]

52. Gamon, J.; Penuelas, J.; Field, C. A narrow-waveband spectral index that tracks diurnal changes in photosynthetic efficiency. *Remote Sens. Environ.* **1992**, *41*, 35–44. [CrossRef]

53. Zarco-Tejada, P.J.; Berjón, A.; López-Lozano, R.; Miller, J.R.; Martín, P.; Cachorro, V.; González, M.; De Frutos, A. Assessing vineyard condition with hyperspectral indices: Leaf and canopy reflectance simulation in a row-structured discontinuous canopy. *Remote Sens. Environ.* **2005**, *99*, 271–287. [CrossRef]

54. Huang, W.; Guan, Q.; Luo, J.; Zhang, J.; Zhao, J.; Liang, D.; Huang, L.; Zhang, D. New Optimized Spectral Indices for Identifying and Monitoring Winter Wheat Diseases. *IEEE J. Sel. Top. Appl. Earth Obs. Remote Sens.* **2014**, *7*, 2516–2524. [CrossRef]

55. Daughtry, C.; Walthall, C.; Kim, M.; De Colstoun, E.B.; McMurtrey Iii, J. Estimating corn leaf chlorophyll concentration from leaf and canopy reflectance. *Remote Sens. Environ.* **2000**, *74*, 229–239. [CrossRef]

56. Gitelson, A.A.; Merzlyak, M.N.; Chivkunova, O.B. Optical properties and nondestructive estimation of anthocyanin content in plant leaves. *Photochem. Photobiol.* **2001**, *74*, 38–45. [CrossRef]

57. Merzlyak, M.N.; Gitelson, A.; Chivkunova, O.B.; Rakitin, V.Y. Non-destructive optical detection of pigment changes during leaf senescence and fruit ripening. *Physiol. Plant.* **1999**, *106*, 135–141. [CrossRef]

58. Filella, I.; Serrano, L.; Serra, J.; Penuelas, J. Evaluating wheat nitrogen status with canopy reflectance indices and discriminant analysis. *Crop. Sci.* **1995**, *35*, 1400–1405. [CrossRef]

59. Haboudane, D.; Miller, J.R.; Tremblay, N.; Zarco-Tejada, P.J.; Dextraze, L. Integrated narrow-band vegetation indices for prediction of crop chlorophyll content for application to precision agriculture. *Remote Sens. Environ.* **2002**, *81*, 416–426. [CrossRef]

60. Zhang, M.; Su, W.; Fu, Y.; Zhu, D.; Xue, J.-H.; Huang, J.; Wang, W.; Wu, J.; Yao, C. Super-resolution enhancement of Sentinel-2 image for retrieving LAI and chlorophyll content of summer corn. *Eur. J. Agron.* **2019**, *111*, 125938. [CrossRef]

61. Zhang, C.; Xie, Z. Combining object-based texture measures with a neural network for vegetation mapping in the Everglades from hyperspectral imagery. *Remote Sens. Environ.* **2012**, *124*, 310–320. [CrossRef]

62. Fu, Y.; Zhao, C.; Wang, J.; Jia, X.; Yang, G.; Song, X.; Feng, H. An Improved Combination of Spectral and Spatial Features for Vegetation Classification in Hyperspectral Images. *Remote Sens.* **2017**, *9*, 261. [CrossRef]

63. Ferreira, M.P.; Wagner, F.H.; Aragão, L.E.; Shimabukuro, Y.E.; de Souza Filho, C.R. Tree species classification in tropical forests using visible to shortwave infrared WorldView-3 images and texture analysis. *ISPRS J. Photogramm. Remote Sens.* **2019**, *149*, 119–131. [CrossRef]

64. Li, S.; Yuan, F.; Ata-Ul-Karim, S.T.; Zheng, H.; Cheng, T.; Liu, X.; Tian, Y.; Zhu, Y.; Cao, W.; Cao, Q. Combining Color Indices and Textures of UAV-Based Digital Imagery for Rice LAI Estimation. *Remote. Sens.* **2019**, *11*, 1763. [CrossRef]

65. Szantoi, Z.; Escobedo, F.; Abd-Elrahman, A.; Smith, S.; Pearlstine, L. Analyzing fine-scale wetland composition using high resolution imagery and texture features. *Int. J. Appl. Earth Obs. Geoinf.* **2013**, *23*, 204–212. [CrossRef]

66. Farwell, L.S.; Gudex-Cross, D.; Anise, I.E.; Bosch, M.J.; Olah, A.M.; Radeloff, V.C.; Razenkova, E.; Rogova, N.; Silveira, E.M.; Smith, M.M.; et al. Satellite image texture captures vegetation heterogeneity and explains patterns of bird richness. *Remote Sens. Environ.* **2021**, *253*, 112175. [CrossRef]

67. Haralick, R.M.; Shanmugam, K.; Dinstein, I. Textural Features for Image Classification. *IEEE Trans. Syst. Man Cybern.* **1973**, *6*, 610–621. [CrossRef]

68. Wang, C.; Wang, S.; He, X.; Wu, L.; Li, Y.; Guo, J. Combination of spectra and texture data of hyperspectral imaging for prediction and visualization of palmitic acid and oleic acid contents in lamb meat. *Meat Sci.* **2020**, *169*, 108194. [CrossRef] [PubMed]

69. Xiong, Z.; Sun, D.-W.; Pu, H.; Zhu, Z.; Luo, M. Combination of spectra and texture data of hyperspectral imaging for differentiating between free-range and broiler chicken meats. *LWT* **2015**, *60*, 649–655. [CrossRef]

70. Liu, D.; Pu, H.; Sun, D.-W.; Wang, L.; Zeng, X.-A. Combination of spectra and texture data of hyperspectral imaging for prediction of pH in salted meat. *Food Chem.* **2014**, *160*, 330–337. [CrossRef]

71. Cen, H.; Lu, R.; Zhu, Q.; Mendoza, F. Nondestructive detection of chilling injury in cucumber fruit using hyperspectral imaging with feature selection and supervised classification. *Postharvest Biol. Technol.* **2016**, *111*, 352–361. [CrossRef]

72. Lu, J.; Zhou, M.; Gao, Y.; Jiang, H. Using hyperspectral imaging to discriminate yellow leaf curl disease in tomato leaves. *Precis. Agric.* **2018**, *19*, 379–394. [CrossRef]

73. Astor, T.; Dayananda, S.; Nidamanuri, R.R.; Nautiyal, S.; Hanumaiah, N.; Gebauer, J.; Wachendorf, M. Estimation of Vegetable Crop Parameter by Multi-temporal UAV-Borne Images. *Remote Sens.* **2018**, *10*, 805. [CrossRef]

74. Li, X.; Zhang, Y.; Luo, J.; Jin, X.; Xu, Y.; Yang, W. Quantification winter wheat LAI with HJ-1CCD image features over multiple growing seasons. *Int. J. Appl. Earth Obs. Geoinf.* **2016**, *44*, 104–112. [CrossRef]

75. Maimaitijiang, M.; Sagan, V.; Sidike, P.; Maimaitiyiming, M.; Hartling, S.; Peterson, K.T.; Maw, M.J.; Shakoor, N.; Mockler, T.; Fritschi, F.B. Vegetation Index Weighted Canopy Volume Model (CVMVI) for soybean biomass estimation from Unmanned Aerial System-based RGB imagery. *ISPRS J. Photogramm. Remote Sens.* **2019**, *151*, 27–41. [CrossRef]

76. Jay, S.; Gorretta, N.; Morel, J.; Maupas, F.; Bendoula, R.; Rabatel, G.; Dutartre, D.; Comar, A.; Baret, F. Estimating leaf chlorophyll content in sugar beet canopies using millimeter- to centimeter-scale reflectance imagery. *Remote. Sens. Environ.* **2017**, *198*, 173–186. [CrossRef]

77. Navrozidis, I.; Alexandridis, T.; Dimitrakos, A.; Lagopodi, A.L.; Moshou, D.; Zalidis, G. Identification of purple spot disease on asparagus crops across spatial and spectral scales. *Comput. Electron. Agric.* **2018**, *148*, 322–329. [CrossRef]

78. Mahlein, A.-K.; Kuska, M.T.; Thomas, S.; Wahabzada, M.; Behmann, J.; Rascher, U.; Kersting, K. Quantitative and qualitative phenotyping of disease resistance of crops by hyperspectral sensors: Seamless interlocking of phytopathology, sensors, and machine learning is needed! *Curr. Opin. Plant. Biol.* **2019**, *50*, 156–162. [CrossRef]

79. Penuelas, J.; Filella, I.; Gamon, J.A. Assessment of photosynthetic radiation-use efficiency with spectral reflectance. *New Phytol.* **1995**, *131*, 291–296. [CrossRef]

80. Rodriguez-Galiano, V.; Chica-Olmo, M.; Abarca-Hernandez, F.; Atkinson, P.M.; Jeganathan, C. Random Forest classification of Mediterranean land cover using multi-seasonal imagery and multi-seasonal texture. *Remote Sens. Environ.* **2012**, *121*, 93–107. [CrossRef]